

Fast and Efficient Detection of 511 keV Photons using Cherenkov Light in PbF₂ Crystal, coupled to a MCP-PMT and SAMPIC Digitization Module.

C. Canot^a M. Alokina^{a,c} P. Abbon^a J.P. Bard^a D. Breton^b E. Delagnes^a J. Maalmi^b
G. Tauzin^a D. Yvon^a and V. Sharyy^{a,1}

^aIRFU, CEA, Université Paris-Saclay, Gif-sur-Yvette, France

^bLAL, IN2P3, CNRS, Université Paris-Saclay, Orsay, France

^cTaras Shevchenko National University of Kyiv, Kyiv, Ukraine

E-mail: viatcheslav.sharyy@cea.fr

ABSTRACT: We study the possibility to use the Cherenkov light for the efficient detection of 511 keV photons with the goal to use it in TOF-PET. We designed and tested two detection modules consisting of PbF₂ crystals attached to Planacon MCP-PMT XP85012. Amplified PMT signals are digitized by the SAMPIC module with high readout rate, up to 10⁵ events/s, and a negligible contribution to the time resolution, below 20 ps (FWHM). We developed a fast 2D scanning system to calibrate the PMT time response and studied in details the timing characteristics of the Planacon PMT.

Using a radioactive ²²Na source we measured a detection efficiency of 24% for 511 keV photons in a 10 mm thick crystal and a coincidence resolving time of 280 ps. We analyzed the main factors limiting the time resolution of the large-surface detection module and proposed solutions to improve it, which will be tested in our future project.

KEYWORDS: Cherenkov Detector, Gamma Detector, Nuclear Imaging, PET, Time-Of-Flight, SAMPIC, Planacon, MCP-PMT

¹Corresponding author

Contents

1	Introduction	1
2	Detection Module and Readout Electronics	2
2.1	Cherenkov Radiator	3
2.2	Photodetector	3
2.3	Readout Electronics	4
3	Efficiency Measurement	6
4	Time Resolution	9
4.1	Dispersion of the Photon Trajectories	10
4.2	Readout Electronics Contribution	10
4.3	PMT Time Resolution	11
5	Coincidence Resolving Time	14
5.1	Measurement	15
5.2	Discussion	17
6	Conclusion	19

Contents

1 Introduction

Positron emission tomography (PET) is a nuclear imaging technique widely used in oncology, cardiology, neurobiology, preclinical researches [1, 2]. PET technique has the ability to image and to quantify biochemical parameters by using specially designed radiopharmaceuticals. All PET tracers incorporate positron emitting, short-living isotopes like ^{18}F , ^{15}O , ^{11}C and others [3, 4]. Annihilation of the emitted positron in the nearby tissue produces mainly two back-to-back 511 keV photons. Detection of both photons in coincidence allows to reconstruct the line-of-response (LOR) and then image the tracer distribution in the object, by recording many coincidence events.

The quality of the image is determined to the large extent by the injected tracer activity and by the signal-to-background ratio. Only several mm in the reconstructed LOR correspond to the annihilation vertex and all other LOR length contributes to the background counts in the reconstruction image. The time-of-flight (TOF) technique allows to reduce efficiently the “background” length of LOR and increase the signal-to-background ratio. It consists in measuring the difference in the detection time of two 511 keV photons and using it as a spatial constraint in the image reconstruction procedure. The TOF reconstruction produces images of better quality with a gain in the

signal-to-noise ratio, G , proportional to δt , the coincidence resolving time (CRT¹). More precisely, $G \simeq D/\Delta x$, where D is a dimension of the object and Δx is a localization uncertainty along LOR, defined as $\Delta x = c\delta t/2$ with c stands for the speed of light in the vacuum, see e.g. [5–11].

The TOF technique has been experimented in PET starting at yearly 80s [7, 12–16], but only during the last decade, the commercial TOF PET scanners reach CRT of 200 – 500 ps [17–23]. Laboratory studies using two detection modules obtain much lower values of CRT, down to ~100 ps for crystals with large thickness, 20 mm typically [24–28], and even 60 ps for crystals of 3 mm thickness [28]. All commercial devices and most of the experimental studies are done using the conventional technique, i.e. bright scintillator coupled to a photo-multiplier tube (PMT) or, recently, to the silicon photo-multiplier. At the same time, this approach is intrinsically limited by the scintillation signal rise and decay time.

Recently, an alternative detection method using the Cherenkov light received more attention. A relativistic electron created by the gamma quantum conversion emits Cherenkov photons at the time scale of several picoseconds, but the number of the emitted photons is very limited, typically 10 – 20. The possibility to use the Cherenkov light in addition to the scintillation and to improve the time resolution is discussed in [29–32] and the improvement is measured experimentally using BGO crystals [33, 34] with CRT values of 200 ps for crystal thickness 3 mm or 330 ps for 20 mm thickness.

Another type of study uses the pure Cherenkov radiator to characterize the possibility to detect 511 keV photons without using scintillation light. Promising results were obtained with lead glass [35, 36], liquid TMBi [37] and crystalline PbF₂ [38–40]. In particular, small PbF₂ crystals coupled to a micro-channel-plate photo-multiplier tube (MCP-PMT) allow to reach a CRT of the order of 85 ps, but with a low detection efficiency of 8 % [39]. The use of the lead glass as a PMT window allows to reach even better CRT of 30 ps, but the detection efficiency “will not satisfy the requirement of clinical PET detector” [36].

In the presented study we investigate the possibility to create a large size PET Cherenkov detection module using a PbF₂ crystal coupled to a commercial MCP-PMT with a large detection efficiency, compatible with the use in PET scanner. We realized and tested two detection modules using fast digitizing electronics, able to provide a high data acquisition rate needed in clinical PET scans and tested their performance using a positrons emitting ²²Nasource.

In the section 2 we describe the detection module assembling and readout electronics, in the section 3 we discuss the detection efficiency measurements and in the section 4 we present the time resolution study, including the detailed investigation of the PMT and readout electronics contribution. The measured CRT and the possible improvements are discussed in the section 5.

2 Detection Module and Readout Electronics

Figure 1 shows the schematic view of the 511 keV photon detection module, consisting of a monolithic PbF₂ crystal with the size 53x53x10 mm³ coupled to a MCP-PMT. To ensure the efficient light collection we use the optical gel OCF452 from Newgate [41] as an optical interface between crystal and PMT window. The detection module is inserted in a black plastic packaging

¹Coincidence Resolving Time: width at half maximum of the time difference distribution.

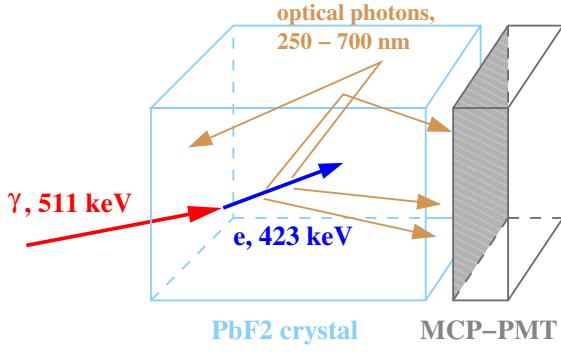


Figure 1: Schematic view of the 511 keV photon detection module with PbF₂ crystal.

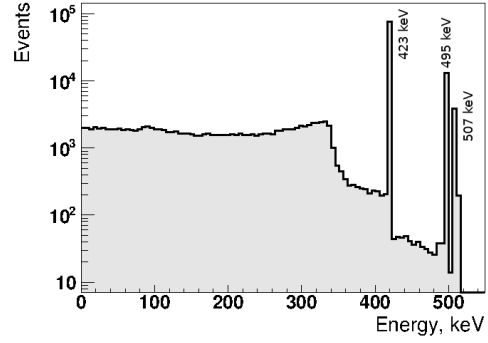


Figure 2: Simulated spectrum of the electron energy produced in the 10 mm PbF₂ crystal by the 511 keV photon conversion. Three peaks correspond to the K, L and M-shell photoionization of lead.

with the 10 mm wall thickness. PMT signals are amplified by commercial amplifiers ZKL and digitized by the module SAMPIC, described later in the section 2.3.

2.1 Cherenkov Radiator

The crystalline lead fluoride, PbF₂, is a non-scintillating crystal transparent to the photon wavelength $\lambda > 250$ nm [42, 43]. Due to its large density, 7.66 g/cm³, and high atomic number of the lead it has a very short attenuation length of 9 mm for 511 keV photons. When such a photon is converted in the crystal via the photoelectric effect (probability 46% [44]), it produces mainly a 423 keV electron. For the other 54%, the photon is converted mainly via the Compton scattering process and produces an electron with energy less than 340 keV, Fig. 2. According to the Geant4 [45, 46] simulation, the detection module with 10 mm crystal has a photon conversion probability of 75%, where 30% corresponds to events with a single photoionization conversion, 20% to events with a single Compton scattering vertex and all other events have at least two vertices, e.g. one Compton and one photoionization vertices or two Compton vertices, etc. Conversion probability of 75% is slightly higher than expectation, 67%, for the the 10 mm-thick crystal with the interaction length 9 mm. This increase is due to the photons generated by the Compton scattering in materials surrounding the detector .

The PbF₂ crystal is an excellent Cherenkov radiator due to the high refraction index of 1.82 at 400 nm wavelength. Electrons emitted through the photoionization process are sufficiently fast to produce about 20 optical photons in average, Fig. 3. Moreover, electrons from the Compton conversion are also producing a smaller number of photons, as shown in Fig. 4. They are contributing to the increase of the overall detection efficiency, but the detection efficiency of events through the Compton scattering is smaller compared to events detected through the photoionization conversion.

2.2 Photodetector

To detect optical photons, we used a MCP-PMT Planacon XP85012 from Photonis [47] with sapphire window. This is a PMT with a bialkali photocathode, 25 μ m micro-channel diameter, active area of

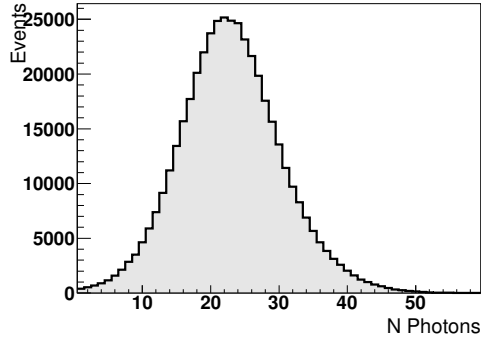


Figure 3: Simulated number of optical photons produced by electron, in the case of photoionization conversion of 511 keV photon.

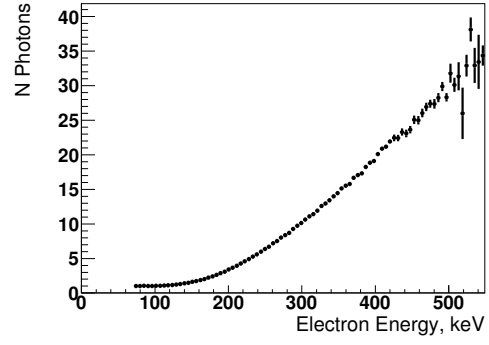


Figure 4: Mean number of Cherenkov photons produced by the electron in PbF_2 crystal versus the electron energy, according to the Geant4 simulation.

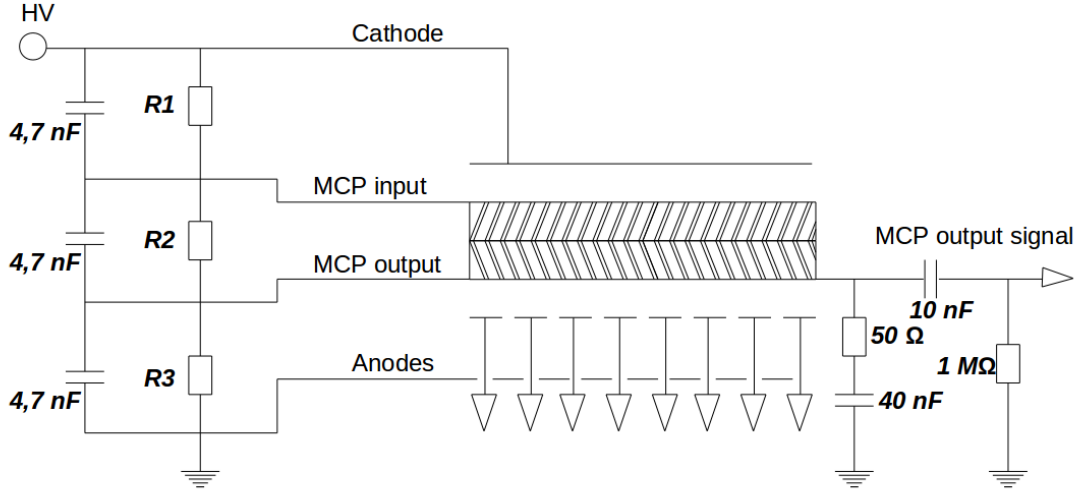


Figure 5: Scheme of the PMT's high voltage divider and signal readout [47].

$53 \times 53 \text{ mm}^2$ and 8×8 anode pad structure, resulting in a pad size of $5.9 \times 5.9 \text{ mm}^2$ and a pitch of 6.5 mm. To operate the PMT, we use the high-voltage divider similar to the recommended one, but with resistance values providing higher voltage between photocathode and MCP: $R1 = 2.2 \text{ M}\Omega$, $R2 = 10 \text{ M}\Omega$, and $R3 = 1 \text{ M}\Omega$, see Fig. 5. We operate the PMT with a high voltage up to 2 kV, which corresponds to a PMT amplification of $1 - 2 \cdot 10^6$ depending on the PMT.

2.3 Readout Electronics

With an amplification of about 10^6 the MCP-PMT provides a single photoelectron signal with an amplitude of several mV. The digitization module SAMPIC, Fig. 6, requires to have a signal in the range of 50 – 1000 mV, such that an additional amplification of PMT signals is necessary. For the Planacon XP85012 we measure a signal rise time of 0.65 ns (10% – 90%) and a typical

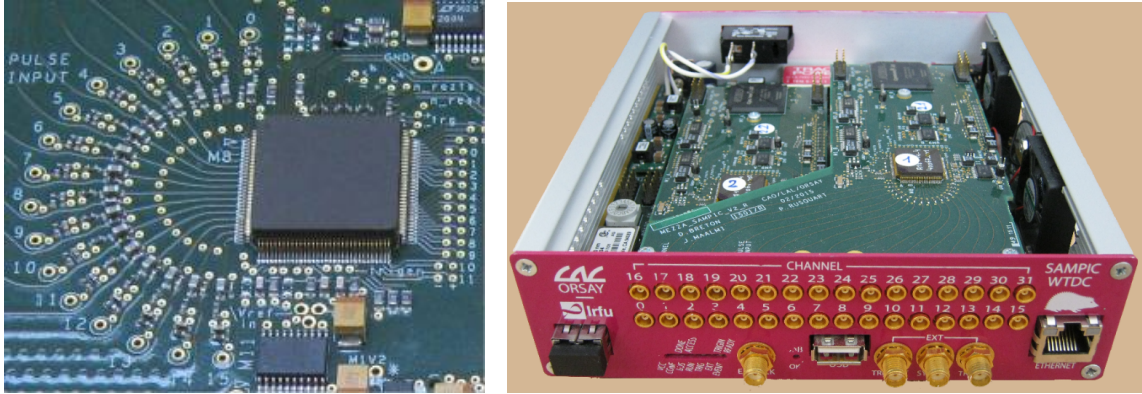


Figure 6: SAMPIC_V3C digitization chip (left) and SAMPIC 32-channel module (right).

signal duration of about 2 ns (FWHM²). In order to preserve the signal shape, an amplifier with a bandwidth of at least 700 MHz is necessary. For the historical reason, we used two types of the commercial amplifiers with 50 Ω input impedance: ZKL-1R5 with amplification 40 dB and bandwidth 1.5 GHz, and ZKL-2R7+ with amplification 24 dB and bandwidth 2.7 GHz. In the described test we were limited to sixteen digitization channels per PMT, such that we developed a customized printed circuit board (PCB), that connects four anodes to one readout channel, as it shown in Fig. 7.

We used one or two detection modules and readout them with the 32-channel SAMPIC module [48, 49]. This SAMPIC module contains two 16-channel SAMPIC_V3C chips, which are based on the concept of Waveform and Time to Digital Converter. Each channel of the chip includes a DLL-based TDC providing a raw time associated with an ultra-fast analog memory sampling of the signals used for waveform recording and precise timing measurement (as good as a few ps RMS). Every channel also integrates a discriminator that can trigger it independently or participate to a more complex trigger, such as “OR” or coincidence between programmable channels. A first trigger level is implemented on-chip while a second trigger level (L2) can be performed at the module level (32 channels). The SAMPIC module provides several sampling frequencies ranging from 1.6 to 8.5 GS/s. It is controlled and readout via an associated data-acquisition software which is used to configure SAMPIC module, start and stop acquisitions, store recorded data on disk in binary or ASCII format and visualize signal waveform and parameter distributions. The SAMPIC module transfers raw signal waveforms to the computer, where all necessary calibrations are applied on-the-fly by the software. In addition, the software performs one of the three hit time extraction algorithms using the waveform data: fixed threshold, constant fraction discriminator (CFD) or multiple CFD. In this work we run at 6.4 GS/s and use the CFD algorithm, as implemented in the SAMPIC software with a 0.5 amplitude fraction. The data to store includes signal waveforms, calculated time and amplitude, and selected SAMPIC parameters. To reduce the required disk space and increase the i/o data rate, the signal waveforms can be omitted in the file recording.

²Full Width at Half Maximum

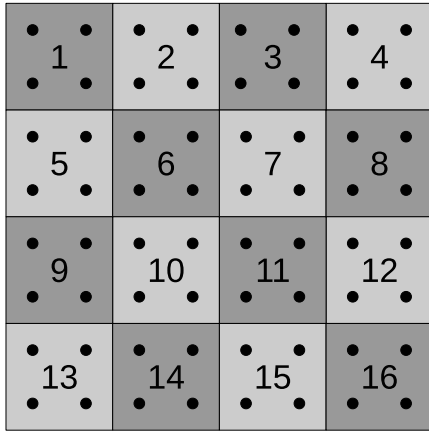


Figure 7: Readout channels numbering. Each point represents one of the 64 PMT anodes. Four anodes are connected to each readout channel.

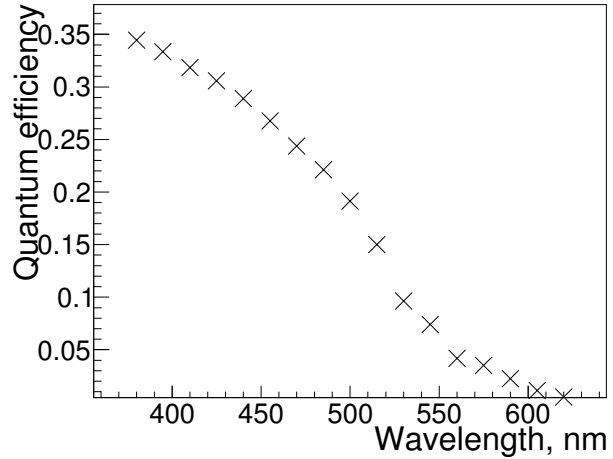


Figure 8: Photocathode efficiency used in Geant4 simulation.

3 Efficiency Measurement

In this work we are studying the feasibility of a PET detection module based on the detection of Cherenkov radiation. Reaching a high efficiency allows to use less annihilation events to obtain good quality image and hence to inject smaller quantity of the radiopharmaceutical and therefore reduces the dose delivered to the patient.

As discuss above (sec. 2.1), the PbF_2 crystal with thickness 10 mm provides a 75% efficiency to convert 511 keV photon. Increased thickness provides higher efficiency, but degrades the time resolution. The photon collection in the crystal depends to a large extend on the quality of the optical interface. The refraction index of the crystal ranged from 1.94 at 300 nm to 1.76 at 600 nm (see e.g. [43]). The optical gel OCF452, used as an optical medium, is transparent for the photons with a wavelength larger than 300 nm and has a refractive index of 1.55 at 400 nm [41]. Due to the significant mismatch between crystal and gel refractive indexes, photons with incident angles more than critical angle $\theta_c = \arcsin(n_{\text{Gel}}/n_{\text{PbF}_2}) \sim 53^\circ$ at 300 nm are reflected (total internal reflection). This reduces the transition probability through the optical interface to the photocathode. To improve the photon collection efficiency it would be better to use an optical medium with higher refraction index. Unfortunately, a general trend observed for optical media is that larger refraction index corresponds to a larger cutoff wavelength. The Cherenkov radiation peaks at blue and ultraviolet values and hence, higher cutoff leads to significant losses of photons with short wavelength. We evaluated the alternative optical “Meltmount Media” with refraction index 1.73 at 400 nm [50] and which is transparent for $\lambda > 400$ nm. The Geant4 simulation shows the same efficiency of 23.1% as for the OCF452 gel, so the improvement in total internal reflection is counterbalanced by the reduced spectral transparency.

The next step in the detection is the conversion of the optical photon to electron(s) in the PMT photocathode. Planacon XP85012 contains a Bialkali photocathode. According to the

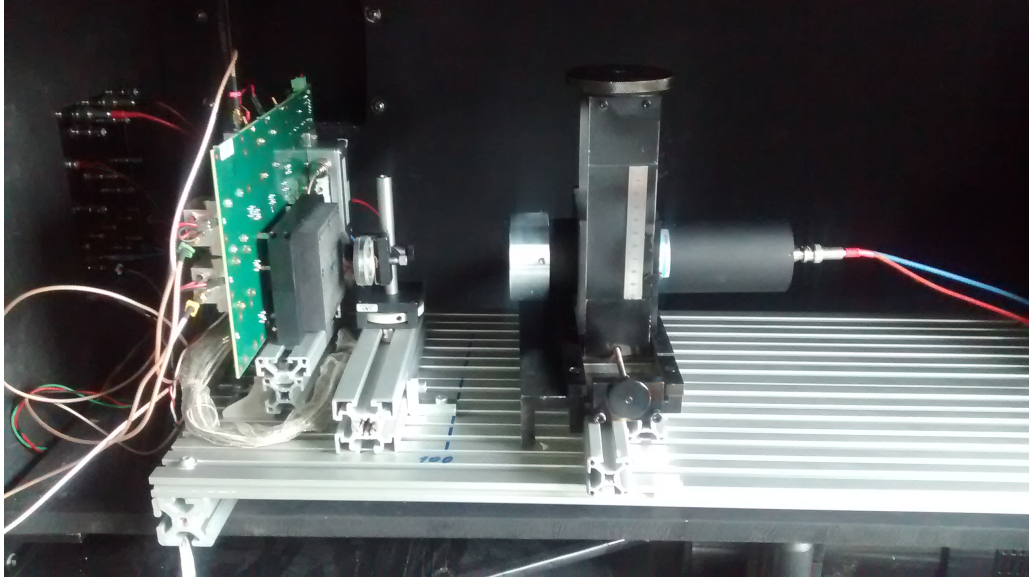


Figure 9: Setup for the detection efficiency measurement. From left to right : the PbF_2 detection module (black squared block) with amplifiers PCB (green plate); the ^{22}Na radioactive source (transparent plastic disk); YAP spectrometer (black cylinder with the metallic ring).

datasheet [47] the highest photocathode quantum efficiency (QE) is of the order of 22% at 380 nm (the Fresnel reflection at the window boundary is taken into account). In the Geant4 simulation we implement the photocathode as a thin metallic layer with the refraction index corresponding to the measurements in [51]. The simulation accounts naturally for the reflection at the windows boundary and for the total internal and Fresnel reflection from the photocathode surface due to its high refraction index (2.7 at 440 nm). We implemented the photocathode quantum efficiency using the datasheet data [47] corrected for the Fresnel reflection both at the interface air-window and window-photocathode, see Fig. 8. Since the details of the photocathode deposition on the sapphire window are not known, the simulation is not expected to reproduce the absolute efficiency with high precision. In addition, the price to pay, when using a MCP-PMT is an extra collection inefficiency for electrons emitted from the photocathode. In the simulation, we assumed a collection efficiency of 60%, typical for these MCP-PMTs, see for example [52, 53]. This value depends on the open-area of the PMT (ratio of channels area to total MCP area) and from the probability of the electron to backscatter from the top of MCP and be collected after that in a pore. In particular, the efficiency to collect the backscattered electrons is limited by the time delay of generated signals, due to the finite duration of the coincidence time window used in the measurement, see section 4.3.

We measure the detection efficiency with the “tag-and-probe” method. For this we use a ^{22}Na radioactive source which emits a positron simultaneously with a 1.27 MeV photon. The positron annihilates with an electron in the encapsulating plastic and produces two 511 keV back-to-back photons. The first 511 keV photon is detected by the “tag” detector, a gamma spectrometer with YAP:Ce crystal. The second 511 keV photon is detected (or not) by the “probe” detector, i.e. by the PbF_2 detection module, see Fig. 9. We calculate the detection efficiency ε in the PbF_2

detection module as:

$$\varepsilon = \frac{N_{PbF_2}}{N_{YAP}}, \quad (3.1)$$

where N_{YAP} is the number of events with 511 keV photon conversion in the YAP spectrometer, and N_{PbF_2} is number of events in PbF_2 detector registered in coincidence with the YAP spectrometer. The distribution of energy deposition measured by the YAP spectrometer is shown in Fig. 10. Only events from range $[511 \text{ keV} - \Delta, 511 \text{ keV} + \Delta]$ are accounted in N_{YAP} , where Δ denotes the half-width of the energy range selection around the photoionization peak, typically 40 keV.

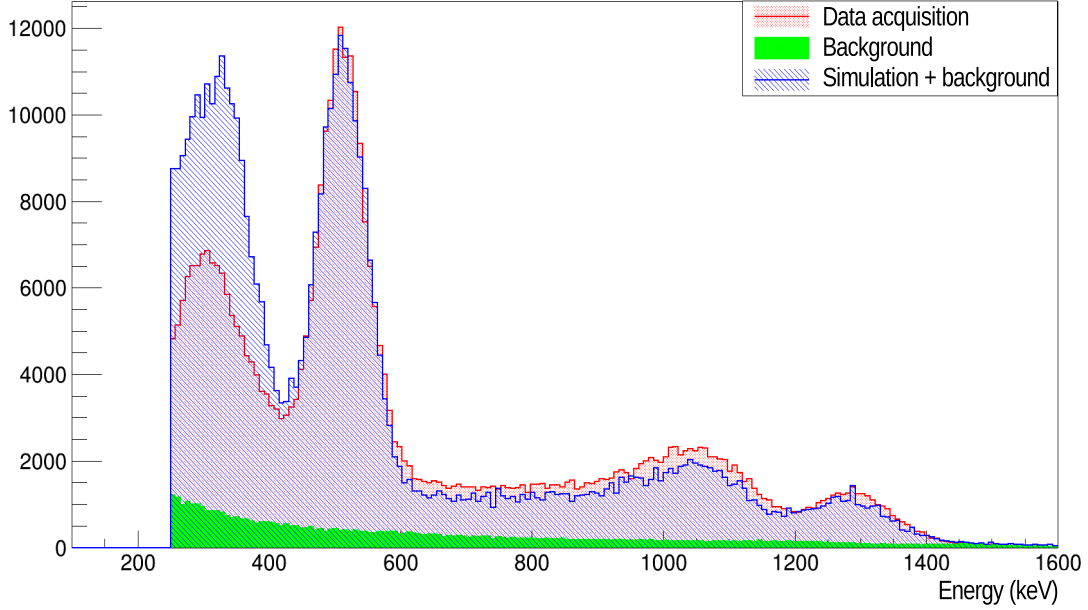


Figure 10: Measured and simulated spectra, produced by a ^{22}Na radioactive source in the YAP spectrometer. The pink histogram is the measured spectrum. The green histogram corresponds to the data collected without any radioactive source. The blue histograms is the energy distribution in simulation added to the spectrum without radioactive source.

Events, recorded with the YAP spectrometer, contain not only signals from 511 keV photon conversion, but also contributions from natural radioactivity and cosmic rays as well as PMT noise. These contributions are quantified by recording spectra without any radioactive source. An additional background contribution is present due to the Compton scattering of 1.27 MeV photon in the YAP spectrometer or in the environment. The corresponding number of events under the 511 keV photon conversion peak is estimated by a simulation where only 1.27 MeV photon present. As one can notice in Fig. 10, the experimental spectrum is not described well by a simulation at values higher than 600 keV and especially at low values. This is because of the environment simulation, i.e. the description of all supporting elements, the metallic test bench, etc. These elements generate additional scattered photons, which are detected by the module. While these events are mainly outside the energy selection range, a small part of them could affect our selection. The observed

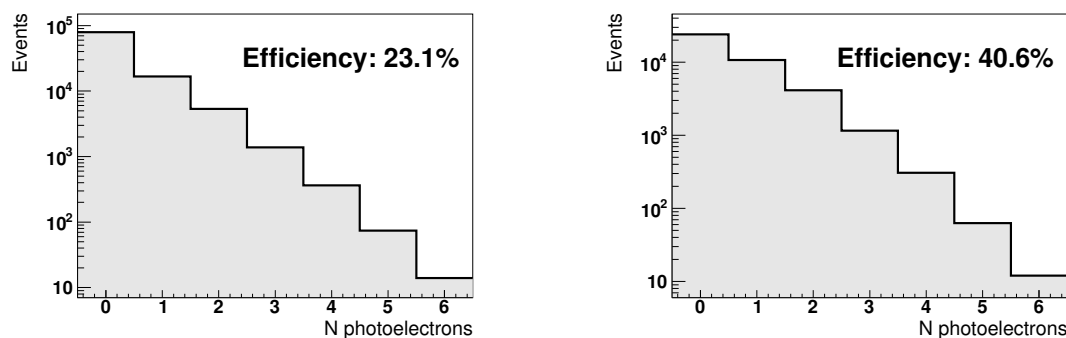


Figure 11: Simulated number of photoelectrons produced at the photocathode (accounting for the photocathode quantum efficiency and photoelectron collection efficiency) for all events (left) or for events, in which the 511 keV photon was converted through the photoionization (right).

mismatch between the blue and the pink histograms above 600 keV is accounted for by adding a systematic uncertainty of $\pm 1\%$.

As the detector does not measure the photon energy deposit, we cannot distinguish events from 511 keV or 1.27 MeV photons. In our test we chose distances to minimize the overlap with 1.27 MeV photon and the remaining contribution is estimated with the Geant4 simulation. We compute a correction factor of 0.940 ± 0.005 .

Finally, taking into account all corrections mentioned above, we compute a global detection efficiency to be:

$$\varepsilon = (23.9 \pm 0.2 \text{ (stat)} \pm 1.0 \text{ (syst)}) \%$$

This number has to be compared with the Geant4 estimation of 23.1%. As mention above, this estimation has significant uncertainties related to the description of the photocathode quantum efficiency and photoelectron collection efficiency. Nevertheless, the measured efficiency is in a good agreement with the simulated one. This number is much higher than obtained in [39] and compatible with use of such system for the PET imaging. This number corresponds to an efficiency of 30% to detect an event if the 511 keV photon is converted in the crystal and of 40% for events converted through the photoelectric conversion process, which is of interest for PET detection. Fig. 11 represents the simulated distribution of the number of photoelectrons generated at the photocathode. As one can see, majority of the detected events have only one or two photoelectrons and hence it is important to optimize the optical photon detection in order to reach higher event detection efficiency.

4 Time Resolution

The expected time resolution for the PbF_2 detection module contains several contributions, which in the case of gaussian distributions, sum up to a standard deviation (SD) σ :

$$\sigma^2 = \sigma_{crystal}^2 + \sigma_{PMT}^2 + \sigma_{jitter}^2 + \sigma_{digit}^2, \quad (4.1)$$

where $\sigma_{crystal}^2$ is a contribution due to the dispersion of the photon trajectories in the crystal, σ_{PMT}^2 is a contribution due to the transit time spread (TTS) of the PMT, σ_{jitter}^2 is a contribution of the

electronics sampling jitter, and σ_{digit}^2 is an electronics contribution proportional to the signal-to-noise ratio divided by the signal risetime. In the following sections we describe each of these contributions and estimate the total time resolution by measuring the time difference between two identical detection modules.

4.1 Dispersion of the Photon Trajectories

To estimate the contribution from the dispersion of the photon trajectories, we use the Geant4 simulation, where we assume negligible PMT TTS and no contribution from the digitization electronics. The time distribution of the first electron emitted by the photocathode is shown in Fig. 12. The FWHM is about 50 ps with a tail due to the Cherenkov photons emitted at large angle, leading to the long travel path with many reflections. For two back-to-back 511 keV photons emitted simultaneously and detected with two identical modules, the distribution in the time difference has CRT of about 76 ps with 30% of events, which are outside ± 100 ps range, Fig. 13

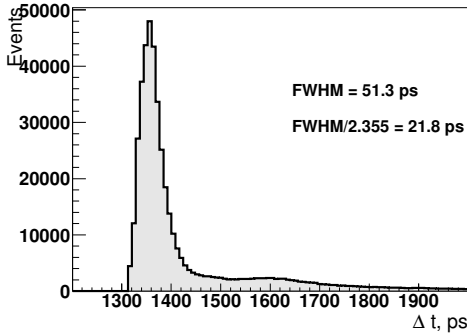


Figure 12: Simulated difference between detection and emission time of 511 keV photon. PMT TTS and electronics time resolution are assumed to be negligible.

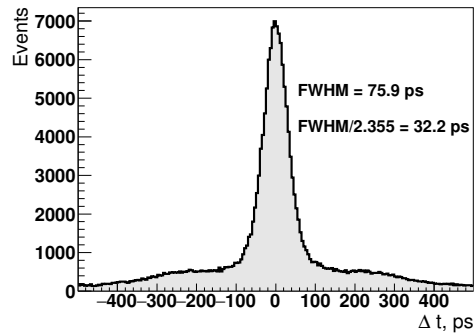


Figure 13: The simulated time difference between detection time of two back-to-back 511 keV photons in two identical PbF_2 modules. PMT TTS and electronics time resolution are assumed to be negligible.

4.2 Readout Electronics Contribution

We distinguish two contributions related to the digitization of the PMT signal: σ_{jitter} and σ_{digit} . For the SAMPIC module the sampling jitter is of the order of $\sigma_{\text{jitter}}^2 \sim 3$ ps (SD) [48]. The σ_{digit} term depends on the noise SD σ_S , which includes contribution from PMT, amplifiers and SAMPIC module and results in a noise for each digitization sample of 1.2 mV. The MCP-PMT generates fast signals with a rise time of 0.65 ns. For a typical signal amplitude of 100 – 500 mV the slope of the rising part of a signal dS/dt is about 0.13 – 0.65 mV/ps, resulting in $\sigma_{\text{digit}} = \sigma_S / (dS/dt) \leq 9 - 2$ ps (SD). As expected, for signals with small amplitudes, the precision is limited by the contribution σ_{digit} , but for the signals with high amplitude, it is limited by the constant term σ_{jitter} . Overall, we expect the contribution of the read-out electronics to the time resolution to be of the order of $\sqrt{\sigma_{\text{jitter}}^2 + \sigma_{\text{digit}}^2} \sim 9.5 - 3.5$ ps (SD), for the signal amplitude between 100 and 500 mV, similar to values reported in [48].

In order to make an independent cross-check of the electronics time resolution, we set-up a dedicated measurement. We use a pulsed laser Pilas by A.L.S. as a light source. The laser beam has a Gaussian-like time profile with duration of about 20 ps (FWHM) and a jitter of 1.4 ps [54]. We place the laser output at 20 mm distance from the PMT window. We chose rather high light intensity, of the order of thousand photoelectrons, and operate the PMT at the moderate high voltage of 1400 V. This results in a stable PMT signal of 150 mV amplitude, amplified to 600 mV in order to match better the SAMPIC range. The histogram in time difference between PMT's signal and laser trigger signal is recorded by the on-line SAMPIC software, see Fig. 14. The obtained distribution is close to a Gaussian with SD 12 ps. The measured value is larger than expected for the signal of 600 mV, but it is obtained with signals from a detector, and possible contribution from the PMT TTS. Additionally, this value contains a contribution from the laser signal jitter, although we expect it to be of the order of several picoseconds, due to the large number of photons in the laser beam.

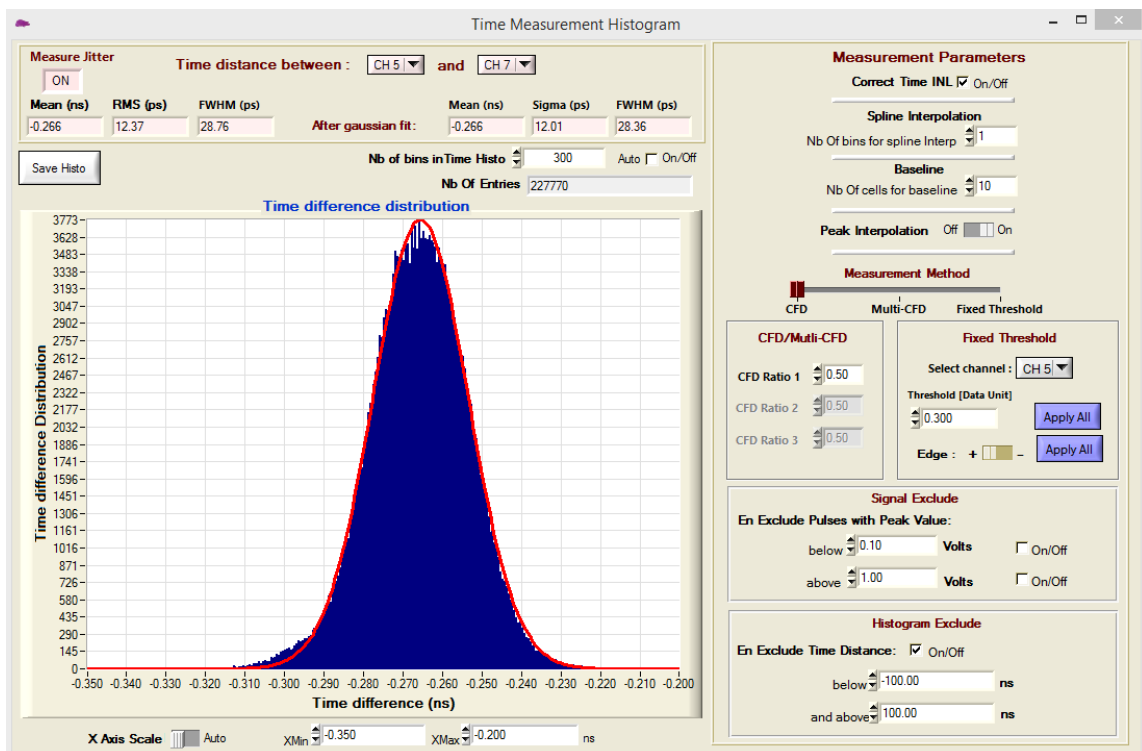


Figure 14: Measured time difference between PMT signal and laser trigger (see text), with the standard deviation of 12 ps, measured by the on-line SAMPIC data acquisition software.

4.3 PMT Time Resolution

As will be seen in the following, the PMT contribution is the main limiting factor in the overall time resolution. To study it in details we build the following system. We use the pulsed laser Pilas [54] collimated by a precise pin-hole of 100 μm diameter. The distance between laser output and pin-hole is about 100 mm and between pin-hole and PMT window is 10 mm. We choose distances and the light intensity in such way that the PMT is working in a single-photon regime with a detection efficiency of 3%. According to the Poisson distribution, this corresponds to a ratio of

two-photons / single-photon events of 1.5%. This number is sufficiently small, that in the following studies we ignore the presence of events with two photons.

The MCP-PMT is mounted at two-axis X-Z motion system, assembled from two X-LRT0100AL-C linear stages from Zaber Technologies Inc. This system allows to move and position the detection module with a precision better than 25 μm [55]. We realized a detector scan with 1 mm step and 1.5 s at each position, which leads to the scan duration of about two hours per PMT. For each position we register amplitude and CFD time of PMT signals from anodes and common cathode, in coincidence with the laser trigger. We use the so-called ‘‘L2 coincidence’’ option of the SAMPIC module, with a 20 ns coincidence time window. The threshold value for anodes signals is 30 mV. Parameters of the laser trigger signal (CFT time and amplitude) are also registered by the SAMPIC module. The data taking rate is between $6 \cdot 10^3$ and $2 \cdot 10^4$ coincidences/s.

Typical time difference distributions between anode signals and laser trigger are shown in Fig. 15. The main part of the distribution has the Gaussian-like shape with FWHM between 85 and 100 ps, Fig. 16b. The tail of the distribution is due to the electrons backscattered from the top of the MCP, see e.g. [56, 57]. We decided to fit this distribution in the range $[-0.4, 1.9]$ ns with the triple-gaussian function:

$$f(t) = \frac{n}{\sqrt{2\pi}} \left(\frac{(1 - f_1 - f_2)}{\sigma_1} e^{-\frac{(t-t_1)^2}{2\sigma_1^2}} + \frac{f_1}{\sigma_2} e^{-\frac{(t-t_1-t_2)^2}{2\sigma_2^2}} + \frac{f_2}{\sigma_3} e^{-\frac{(t-t_1-t_3)^2}{2\sigma_3^2}} \right), \quad (4.2)$$

where n is a normalization coefficient, f_1 , f_2 are fractions of events in second and third Gaussian terms representing the tail of the distribution, t_1 is the mean of the first term, t_2 , t_3 are the additional delays in mean for second and third terms, σ_1 , σ_2 , σ_3 are the corresponding standard deviations. The typical mean value for the first gaussian is $t_1 \simeq -80$ ps, so the backscattered electrons with delay up to $t_2 \simeq 2$ ns contribute to the fit. As can be seen in Fig. 15, the function 4.2 fit well the main peak, but tail is not described perfectly. Nevertheless, we used this function, because it has the advantage to be simple and characterizes reasonably well the main features of the distribution.

For each position, the time difference is fitted using the function 4.2 and the obtained parameters are plotted as 2D histograms versus x and y coordinates. Several such histograms are presented in Figs. 16 and 17 for one of the PMTs. For example, Fig. 16a shows the number of channels with signals above 50 mV threshold. One clearly identifies regions in the detector where only one channel is triggered at once, but at the border between two channels, the two are triggered at the same time (in this case, we use the earliest signal time among all triggered as a PMT time). This happens due to the so-called charge sharing effect, when the electron shower induces signals simultaneously on two anode electrodes, see e.g. [56–58]. We observe that charge sharing happens at the distance of 1-2 mm from the pad edge. The cross-talk due to the capacitive coupling between anodes could cause the similar effects, but it affects anode pairs independent of the event position [59, 60]. For the pixel at the center of anodes, we observe 2.5% of events with two channels triggered simultaneously, so the effect of capacitive coupling is rather small. Additionally, these cross-talk pulses have a differential shape. To speed-up the data taking during the scan, we do not register the pulse shape, so we could not apply any shape selection. In tests with a radioactive source, we register the shape of the signal and apply additional selection to reduce even more the fraction of cross-talk signals due to the capacitive coupling.

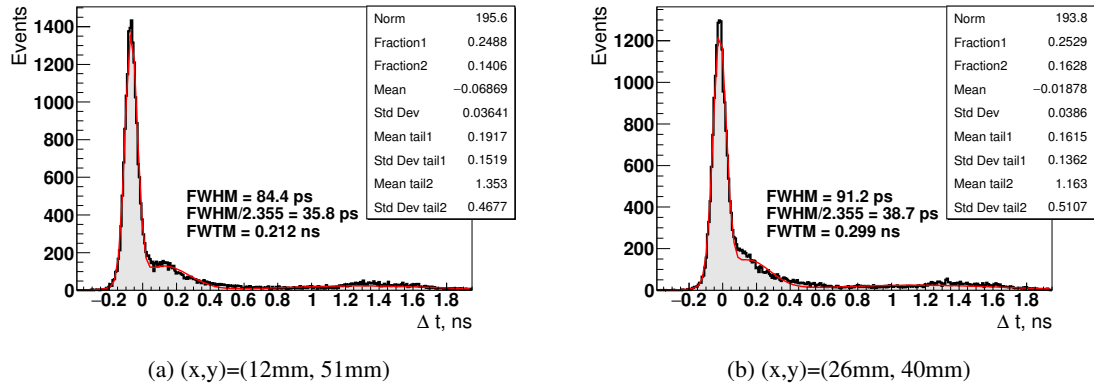


Figure 15: Typical difference in time between PMT anode signal and laser trigger measured at two different positions. The red line represents the triple-gaussian fit function. The FWHM and FWTM (full width at tens of maximum) are calculated using the histogram and independently from the fit function.

Fig. 16b shows that the FWHM of the peak is rather uniform through the entire PMT surface and has typical value of 85 – 90 ps. At the border between two channels the time resolution is degrading to 100 – 110 ps due to the charge sharing effect, but we did not observe any degradation at the border of two anodes when they are connected to the same readout channel. This degradation could not be attributed to the signal time walk effect, because we use the CFD algorithm for time calculation. It rather reflects the more complex interplay between the charge sharing mechanism and anode signal formation. The worse resolution observed for the readout channel with coordinates $(x,y) = (7-19 \text{ mm}, 33-46 \text{ mm})$ is attributed to an imperfection in the readout PCB design, since we observed it for two different PMTs. The fraction of events with the time difference $t - t_1$ larger than 100 ps is around 25%, but with a degradation in the corner of the PMT, Fig. 16c. Such degradation is observed only for one PMT among the two tested.

A 2D distribution of the t_1 parameter is shown in Fig. 17a. We observe an important dispersion of the order of 50–80 ps inside individual readout channel. Over a single anode pad (we connect 4 anodes in one readout channel), this dispersion is smaller, but still present. In order to obtain the optimal performance from the detector, the signal propagation delays should be calibrated and taken into account. Unfortunately, the current readout scheme has no means to make the exact correspondence between an event and (x,y) coordinates. The dispersion of the delays inside each channel is an important and irreducible limitation for obtaining the optimal performance from the device in the current readout design. Fig. 18 shows the distribution of time difference per channel. The width of the distribution is significantly larger, compared to the per-position distribution (Fig. 15), typically 105 – 145 ps, see Tab. 1. Central channels have better performance due to the smaller dispersion in the t_1 parameter. Due to the charge sharing effects, we observe the correlation between the mean and the signal amplitude, so for further test we apply a calibration of delays (t_1 parameter) versus signal amplitude, individually for each channel.

The common cathode signal could be used as a sum of all anode signals, for example, for triggering. Due to the large capacity of the cathode, the signal is slower and smaller than a typical

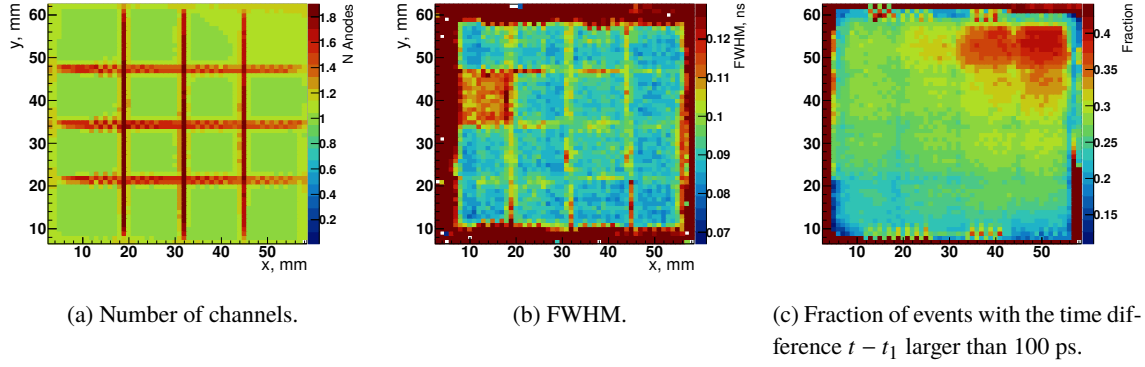


Figure 16: Measured parameters of the time difference distribution as a function of the (x,y) coordinates during the laser scan.

anode signal. Nevertheless it allows to reach a reasonable resolution in time with a typical FWHM of 120 – 180 ps for a fixed position. The Fig. 17b shows the peak timing (parameter t_1 in the Eq. (4.2)) for the cathode signal as a function of (x,y) coordinates. As one can see, the signal needs around 250 ps to arrive from the far end of the electrode to the point of the signal readout.

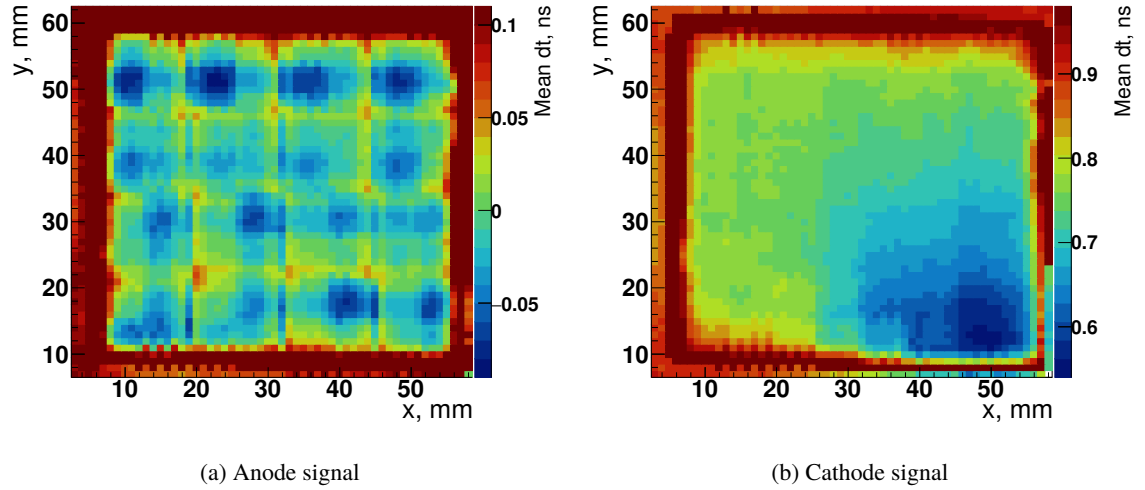


Figure 17: Measured peak timing (parameter t_1 , in the Eq. (4.2)) as a function of the (x,y) coordinates.

5 Coincidence Resolving Time

According to Eq. (4.1) we expect to reach the time resolution per detector of about 50 ps (SD) in the best case, corresponding to the CRT values of 170 ps. As will be demonstrated in the following, this expectation is optimistic, in particular due to the presence of the non-gaussian tail in distributions of the photon trajectories dispersion and the PMT timing resolution.

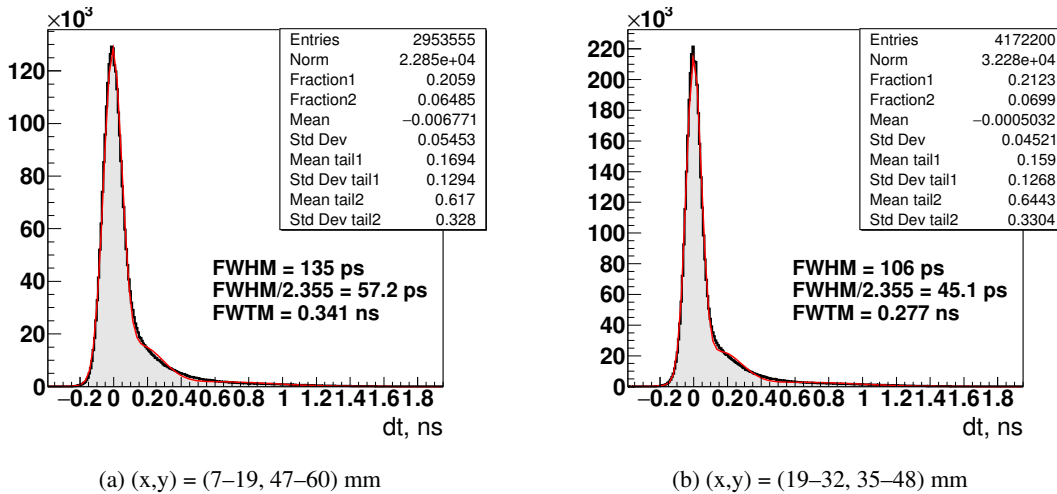


Figure 18: Per-channel distribution for time difference between PMT signal and laser trigger for two selected channels.

Channel y \ Channel x	Channel x			
	7 – 19 mm	20 – 32 mm	33 – 45 mm	46 – 58 mm
48 – 60 mm	148	137	146	135
35 – 47 mm	119	108	106	134
22 – 34 mm	110	115	120	118
9 – 21 mm	120	132	121	133

Table 1: FWHM per channel (ps) for the time difference distribution (see text).

5.1 Measurement

To measure the time resolution we use two detector modules described in the section 2. Two detectors are installed front-to-front on the optical bench at a distance of 76 cm between them. In the center, we place a ^{22}Na radioactive source with a thin, disk-like active area of 10 mm diameter, encapsulated in 10 mm thick plexiglass disk. With such configuration, the probability of simultaneous detection of 1.27 MeV and 511 keV photons is less than 0.3% and the obtained results could be interpreted as the CRT for detecting two back-to-back 511 keV photons. We readout both detectors using a 32-channel SAMPIC module and the coincidence trigger is realized by the module itself. In particular, we register all events where any anode signal from one PMT is in coincidence with any anode signal from another PMT within the time window of 20 ns. Typical recorded signals are shown in Fig. 19. The data acquisition rate is about 400 coincidences/s. The measured random coincidence rate due to the dark count rate of PMTs is 4.7 coincidences/s, but these events are uniformly distributed in the range $[-10 \text{ ns}, 10 \text{ ns}]$ and, hence, represent only a negligible fraction of events, 0.1%, in the signal region $[-1 \text{ ns}, 1 \text{ ns}]$.

The distribution for the measured difference in time is shown in Fig. 20, where we chose 30 mV threshold for the PMT with the amplification 24 dB and 100 mV for the PMT with the amplification

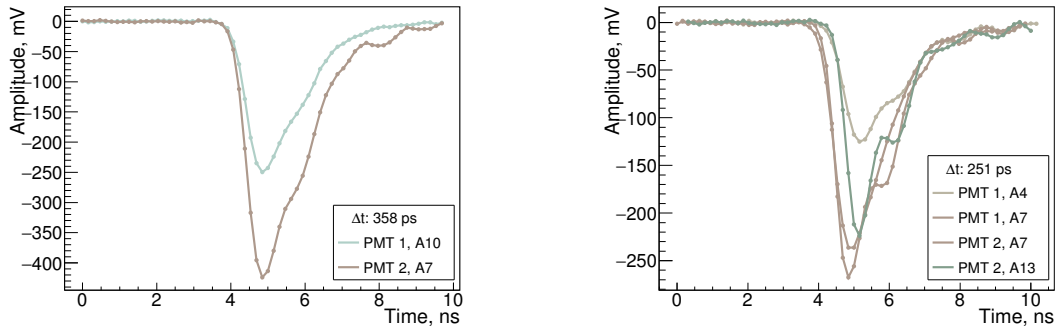


Figure 19: Example of signals registered in coincidence by two detection modules.

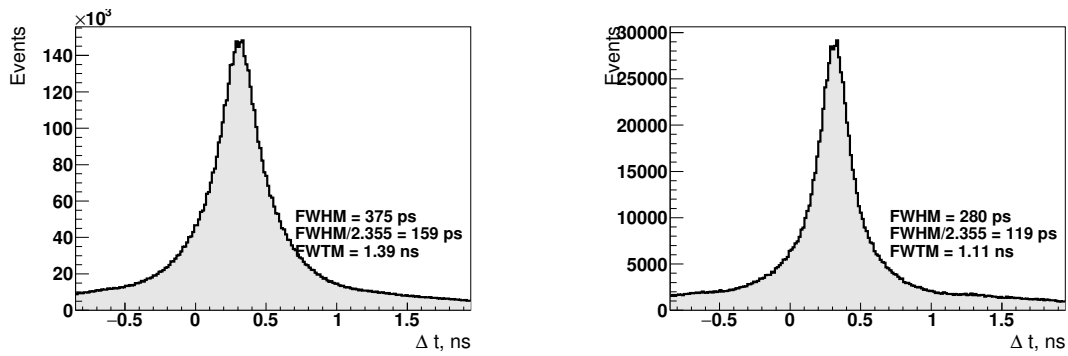


Figure 20: Measured difference in time between two detection modules for the full surface (left) or 4 central channels only (right).

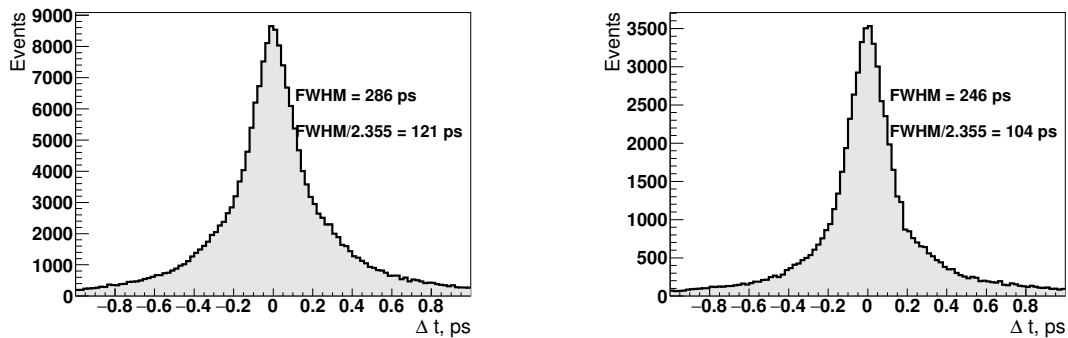


Figure 21: Simulated difference in time between two detection modules for the full surface (left) or 4 central channels only (right).

40 dB. As seen on these pictures, the measured CRT is worse for the full surface of the PMT, than for the central channels only. The difference is caused mainly by the finite size of the radioactive source active area (diameter 10 mm) leading to a higher efficiency to detect coincidence by the central channels compare to the peripheral ones. In consequence, the peripheral channels have large fraction of events triggered by the photons reflected several times in the crystal and, hence, worse time resolution.

Simulated distributions show 14% better resolution for the central channels and 30% better for the full surface, see Fig. 21. It could be explained by the fact, that quality of the surface has an important role for the simulation of the photon reflection inside the crystal. We used crystals with the surfaces polished to optical quality, but the actual quality is not measured. The results presented in Fig. 21 are simulated using Geant4 UNIFIED model [61] assuming the Gaussian distribution of the photon direction due to reflection from the micro-facets with a standard deviation of 0.1° . We set the specular lobe probability to one and all others (specular spike, backscatter and Lambertian) to zero. Any difference in surface simulation with the real surfaces quality will affect mainly the peripheral channels.

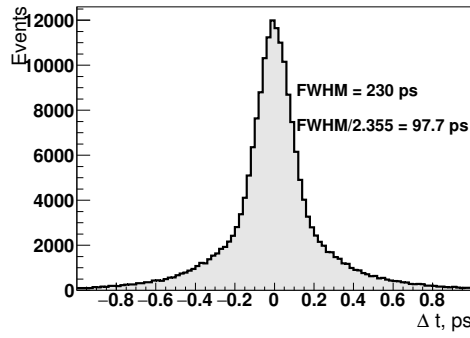
5.2 Discussion

In this study we demonstrated the possibility to build a Cherenkov based crystalline detector for 511 keV photons. Due to high density and high atomic number of the PbF_2 crystal, as well as the large detection surface, such a detector provides an efficiency of 24% suitable for building a TOF-PET scanner. For example, using the crystal matrix made with $6 \times 6 \times 10 \text{ mm}^3$ PbF_2 crystals attached to the MCP-PMT, one can design the whole body Cherenkov PET scanner, with performance comparable to conventional scanners, as estimated by the simulation with somewhat optimistic hypothesis [62, 63].

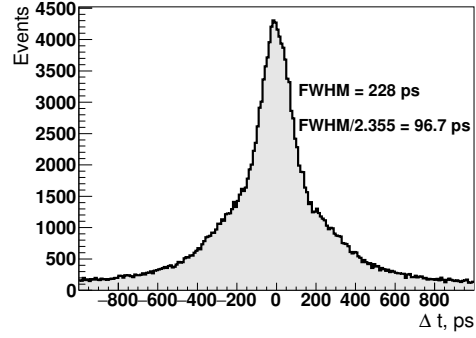
Nevertheless, the performance of such a detection module stays modest due to the several limitations. First of all, the obtained CRT exceeds a lot the gaussian expectation $\sqrt{2}\sigma_{\text{detector}}$ due to the presence of non-gaussian tails in the distributions. These tails are due to the dispersion of the photon trajectories and especially due to the MCP backscattered electrons, which generate delayed signals for at least 25% of events in the range of 100 – 2000 ps (for Planacon XP85012). Any reduction in the fraction of such events will improve significantly the CRT. For example, in Fig. 22a we shows the simulated distribution of the time difference between two detection module, where we remove the tail in PMT resolution function by assigning parameters f_1 and f_2 from eq. 4.2 to zero. This distribution has smaller width by about 20% compare to the Fig. 21.

As mentioned in the section 4.3, the dispersion of the signal delays inside one channel requires the use of small pads individually readout, but small pads increase the fraction of events affected by the charge sharing effects. Ideally, a continuous readout with the possibility to reconstruct x and y position of each photon allows to calibrate and correct for delays, so improving the time resolution. Fig. 22b shows the distribution of the time difference between two detection module, assuming no degradation from the signal delays inside channels. As expected, the CRT is improved by 20% compared to Fig. 21.

The main disadvantage in using the Cherenkov radiation compare to the scintillation is the small number of generated photons and detected photoelectrons. An increase in the number of photoelectrons generated at the photocathode will improve very significantly the time resolution.



(a) Without tail in the PMT resolution function.



(b) No degradation from the dispersion of signal delays inside channel.

Figure 22: Simulated time difference between two detection modules with modified PMT resolution function.

For example, Planacon XP85012 PMT features a bi-alkali photocathode with a maximum efficiency of 22% [47], but better photocathodes with efficiency up to 30% are available now [64]. An important loss in efficiency is also caused by the non-ideal optical interface as described in the section 3 and reflection of Cherenkov photons with a large incident angle from the crystal border. Increasing the critical angle would increase the number of the detected optical photons. In addition, it reduces the number of photon reflections in the crystal, and thus will improve the time resolution. To increase the critical angle, one needs to increase the refraction index of the external media. The conventional way to do so is to apply the optical media between PMT and crystal. Unfortunately, it is not possible to find an optical media with high refraction index, and, simultaneously, transparent in the deep UV region, required for the detection of Cherenkov photons. An alternative way to improve the optical interface, proposed by us previously [65], is to use a molecular bonding between crystal and PMT window. This procedure glues together PMT window and crystal without using any intermediate media. If the PMT window has a high refractive index (e.g. sapphire), it will significantly improve the quality of the optical interface. Such an operation requires polishing of both surfaces to the roughness less than 1 nm and planarity below 1 μm . In addition, both surfaces should be free of dust particles or contamination, especially hydrocarbons, see e.g. [66]. This technique was judged to be too challenging, especially taking into account the necessity prepare a photocathode on the bounding object under the ultra-high vacuum and high temperature.

Finally, we decided to improve the optical interface by removing completely the border between PMT window and a Cherenkov radiator and depose photocathode directly on the crystal. We choose to implement this technique using the PbWO_4 crystal, which is almost as good Cherenkov radiator as PbF_2 and, in addition, produces a small number of fast scintillating photons. This idea is the main element of our future project named ClearMind [67].

6 Conclusion

In this paper we studied the possibility to construct a Cherenkov PET detection module with high efficiency and good timing performance using PbF₂ crystal and commercial MCP-PMT. We measured an efficiency of 24% to detect a 511 keV photon in a 10 mm thick crystal. This value is sufficiently high to be used in PET if high TOF resolution is reached. The use of SAMPIC fast digitization module allows to minimize the electronics contribution to the time resolution to the level below 20 ps (FWHM) and provides the high rate readout capability of up to 10⁵ events/s. We developed the fast scanning system to calibrate the time response of the PMT and used it for precise calibration of Planacon XP85012. We observe a good time response for the entire PMT surface with the resolution of about 90 ps (FWHM) and the presence of delayed events in the range of 100 – 2000 ps at the level of 25%.

Finally, we measured the CRT between two identical modules of about 280 ps, limited by the low number of detected optical photons, the PMTs performances and the implemented readout scheme. The time resolution, reachable with the proposed approach, limits the potential of such technique for full-size scanner.

We are working on an improvement of the detection module performance by improving the optical interface between PMT window and crystal and by improving the PMT readout scheme.

Acknowledgments

We thank the Photonis representative Serge Duarte Pinto for constructive discussions on MCP-PMT technology.

We acknowledge the financial support by the LabEx P2IO R&D project of the region Ile-de-France, the "IDI 2015" project funded by the IDEX Paris-Saclay, ANR-11-IDEX-0003-02, the PhD financial support by the French embassy in Ukraine, DRI University Paris-Saclay and the Programme Transversal Technologies pour la Santé, of CEA. This work is conducted in the scope of the IDEATE International Associated Laboratory.

References

- [1] C. Kuntner and D. B. Stout, *Quantitative preclinical PET imaging: opportunities and challenges*, *Frontiers in Physics* **2** (2014) .
- [2] S. Walrand, M. Hesse and F. Jamar, *Update on novel trends in PET/CT technology and its clinical applications*, *British Journal of Radiology* **91** (2016) 20160534.
- [3] V. W. Pike, *PET radiotracers: crossing the blood brain barrier and surviving metabolism*, *Trends in Pharmacological Sciences* **30** (2009) 431–440.
- [4] S. Vallabhajosula, L. Solnes and B. Vallabhajosula, *A Broad Overview of Positron Emission Tomography Radiopharmaceuticals and Clinical Applications: What Is New?*, *Seminars in Nuclear Medicine* **41** (2011) 246–264.
- [5] R. Campagnolo, P. Garderet and J. Vacher, *Tomographie par émetteurs positrons avec mesure de temps de vol*, In *Proc. Commun. au Colloque National sur le Traitement du Signal, Nice, France* (May 1979) .

- [6] T. Tomitani, *Image Reconstruction and Noise Evaluation in Photon Time-of-Flight Assisted Positron Emission Tomography.*, *IEEE Transactions on Nuclear Science* **28** (1981) 4581.
- [7] M. Yamamoto, D. C. Ficke and M. M. Ter-Pogossian, *Experimental Assessment of the Gain Achieved by the Utilization of Time-of-Flight Information in a Positron Emission Tomograph (Super PETT I)*, *IEEE Transactions on Medical Imaging* **1** (1982) 187–192.
- [8] T. F. Budinger, *Time-of-Flight Positron Emission Tomography: Status Relative to Conventional PET*, *Journal of Nuclear Medicine* **24** (1983) 73.
- [9] M. Conti, *Focus on time-of-flight PET: the benefits of improved time resolution*, *European Journal of Nuclear Medicine and Molecular Imaging* **38** (2011) 1147–1157.
- [10] P. Geramifar, M. Ay, M. S. Zafarghandi, S. Sarkar, G. Loudos and A. Rahmim, *Investigation of time-of-flight benefits in an LYSO-based PET/CT scanner: A Monte Carlo study using GATE*, *Nuclear Instruments and Methods in Physics Research, Section A* **641** (2011) 121–127.
- [11] V. Westerwoudt, M. Conti and L. Eriksson, *Advantages of Improved Time Resolution for TOF PET at Very Low Statistics*, *IEEE Transactions on Nuclear Science* **61** (2014) 126–133.
- [12] R. Allemand, C. Gresset and J. Vacher, *Potential Advantages of a Cesium Fluoride Scintillator for a Time-of-Flight Positron Cameras*, *Journal of Nuclear Medicine* **21** (1980) 153–155.
- [13] M. J. Vacher, R. Allemand, M. M. Laval, M. Moszynski and R. Odru, *New Development on Detection at Fast Timing on the Time-of-Flight LETI Device*, *Proceedings of the Workshop on Time-of-Flight Tomography*, Washington University: IEEE Publication (1982) 143–146.
- [14] M. Ter-Pogossian, D. Ficke, M. Yamamoto and J. Hood, *Super PETT I: A Positron Emission Tomograph Utilizing Photon Time-of-Flight Information*, *IEEE Transactions on Medical Imaging* **1** (1982) 179–187.
- [15] B. Bendriem, F. Soussaline, R. Campagnolo, B. Verrey, P. Wajnberg and A. Syrota, *A Technique for Scattered Event Compensation in a PET System Using TOF Information*, *Information Processing in Medical Imaging: Proceedings of the 9th conference, Washington D.C., 10–14 June 1985* (1986) 475–480.
- [16] R. Trebossen and B. Mazoyer, *Contrate Performances Of TTV03, The CEA-LETI Time-of-Flight Positron Emission Tomograph.*, *1990 IEEE Nuclear Science Symposium Conference Record* (1990) 1257–1262.
- [17] S. Surti, A. Kuhn, M. E. Werner, A. E. Perkins, J. Kolthammer and J. S. Karp, *Performance of Philips Gemini TF PET/CT Scanner with Special Consideration for Its Time-of-Flight Imaging Capabilities*, *Journal of Nuclear Medicine* **48** (2007) 471–480.
- [18] B. W. Jakoby, Y. Bercier, M. Conti, M. E. Casey, B. Bendriem and D. W. Townsend, *Physical and Clinical Performance of the mCT Time-of-Flight PET/CT Scanner*, *Physics in Medicine and Biology* **56** (2011) 2375–2389.
- [19] V. Bettinardi, L. Presotto, E. Rapisarda, M. Picchio, L. Gianolli and M. C. Gilardi, *Physical Performance of the New Hybrid PET/CT Discovery-690*, *Medical Physics* **38** (2011) 5394–5411.
- [20] H. Zaidi, N. Ojha, M. Morich, J. Griesmer, Z. Hu, P. Maniawski et al., *Design and performance evaluation of a whole-body Ingenuity TF PET–MRI system*, *Physics in Medicine and Biology* **56** (2011) 3091–3106.
- [21] M. Miller, J. Zhang, K. Binzel, J. Griesmer, T. Laurence, M. Narayanan et al., *Characterization of the Vereos Digital Photon Counting PET System*, *Journal of Nuclear Medicine* **56** (2015) 434.

- [22] L. Huo, N. Li, H. Wu, W. Zhu, H. Xing, J. Ba et al., *Performance evaluation of a new high-sensitivity time-of-flight clinical PET/CT system*, *EJNMMI Physics* **5** (2018) 29.
- [23] J. van Sluis, J. de Jong, J. Schaar, W. Noordzij, P. van Snick, R. Dierckx et al., *Performance Characteristics of the Digital Biograph Vision PET/CT System*, *Journal of Nuclear Medicine* **60** (2019) 1031–1036.
- [24] H. T. van Dam, G. Borghi, S. Seifert and D. R. Schaart, *Sub-200 ps CRT in monolithic scintillator PET detectors using digital SiPM arrays and maximum likelihood interaction time estimation*, *Physics in Medicine and Biology* **58** (2013) 3243.
- [25] G. Borghi, V. Tabacchini and D. R. Schaart, *Towards monolithic scintillator based TOF-PET systems: practical methods for detector calibration and operation*, *Physics in Medicine and Biology* **61** (2016) 4904–4928.
- [26] E. Berg and S. R. Cherry, *Using convolutional neural networks to estimate time-of-flight from PET detector waveforms*, *Physics in Medicine and Biology* **63** (2018) 02LT01.
- [27] J. W. Cates and C. S. Levin, *Evaluation of a clinical TOF-PET detector design that achieves ≤ 100 ps coincidence time resolution*, *Physics in Medicine and Biology* **63** (2018) 115011.
- [28] S. Gundacker, R. M. Turtos, E. Auffray, M. Paganoni and P. Lecoq, *High-frequency SiPM readout advances measured coincidence time resolution limits in TOF-PET*, *Physics in Medicine and Biology* **64** (2019) 055012.
- [29] P. Lecoq, E. Auffray, S. Brunner, H. Hillemanns, P. Jarron, A. Knapitsch et al., *Factors Influencing Time Resolution of Scintillators and Ways to Improve Them*, *IEEE Transactions on Nuclear Science* **57** (2010) 2411–2416.
- [30] S. Brunner, L. Gruber, J. Marton, K. Suzuki and A. Hirtl, *New approaches for improvement of TOF-PET*, *Nuclear Instruments and Methods in Physics Research, Section A* **732** (2013) 560–563.
- [31] S. E. Brunner, L. Gruber, J. Marton, K. Suzuki and A. Hirtl, *Studies on the Cherenkov Effect for Improved Time Resolution of TOF-PET*, *IEEE Transactions on Nuclear Science* **61** (2014) 443–447.
- [32] P. Lecoq, *Pushing the Limits in Time-of-Flight PET Imaging*, *IEEE Transactions on Radiation and Plasma Medical Sciences* **1** (2017) 473–485.
- [33] S. I. Kwon, A. Gola, A. Ferri, C. Piemonte and S. R. Cherry, *Bismuth germanate coupled to near ultraviolet silicon photomultipliers for time-of-flight PET*, *Physics in Medicine and Biology* **61** (2016) L38–L47.
- [34] S. E. Brunner and D. R. Schaart, *BGO as a hybrid scintillator / Cherenkov radiator for cost-effective time-of-flight PET*, *Physics in medicine and biology* **62** (2017) 4421–4439.
- [35] M. Miyata, H. Tomita, K. Watanabe, J. Kawarabayashi and T. Iguchi, *Development of TOF-PET using Cherenkov Radiation*, *Journal of Nuclear Science and Technology* **43** (2006) 339–343.
- [36] R. Ota, K. Nakajima, I. Ogawa, Y. Tamagawa, H. Shimoi, M. Suyama et al., *Coincidence time resolution of 30 ps FWHM using a pair of Cherenkov-radiator-integrated MCP-PMTs*, *Physics in Medicine and Biology* **64** (2019) 07LT01.
- [37] E. Ramos, D. Yvon, P. Verrecchia, G. Tauzin, D. Desforge, V. Reithinger et al., *Trimethyl Bismuth Optical Properties for Particle Detection and the CaLIPSO Detector*, *IEEE Transactions on Nuclear Science* **62** (2015) 1326–1335.
- [38] S. Korpar, R. Dolenc, P. Križan, R. Pestotnik and A. Stanovnik, *Study of TOF PET using Cherenkov light*, *Nuclear Instruments and Methods in Physics Research, Section A* **654** (2011) 532–538.

- [39] S. Korpar, R. Dolenc, P. Križan, R. Pestotnik and A. Stanovnik, *Study of a Cherenkov TOF-PET module*, *Nuclear Instruments and Methods in Physics Research, Section A* **732** (2013) 595–598.
- [40] R. Dolenc, S. Korpar, P. Križan, R. Pestotnik and N. Verdel, *The Performance of Silicon Photomultipliers in Cherenkov TOF PET*, *IEEE Transactions on Nuclear Science* **63** (2016) 2478–2481.
- [41] Newgate Simms Limited, *Technical Data Sheet for OCF-452*, tech. rep., 2015.
- [42] W. S. C. Williams and H. S. Caplan, *A Lead Fluoride Total-Absorption Spectrometer for High-Energy Electrons and Photons*, *Nature* **179** (1957) 1185–1186.
- [43] D. Anderson, M. Kobayashi, Y. Yoshimura and C. Woody, *Lead Fluoride: An Ultracompact Cherenkov Radiator for EM Calorimetry*, *Nuclear Instruments and Methods in Physics Research, Section A* **290** (1990) 385.
- [44] M. Berger, J. Hubbell, S. Seltzer, J. Chang, J. Coursey, R. Sukumar et al., *XCOM: Photon Cross Sections Database. NIST Standard Reference Database 8 (XGAM)*, tech. rep., 2010. doi: 10.18434/T48G6X.
- [45] GEANT4 collaboration, S. Agostinelli et al., *GEANT4: A Simulation toolkit*, *Nuclear Instruments and Methods in Physics Research, Section A* **506** (2003) 250–303.
- [46] J. Allison, K. Amako, J. Apostolakis, H. Araujo, P. Dubois et al., *Geant4 developments and applications*, *IEEE Transactions on Nuclear Science* **53** (2006) 270.
- [47] Photonis, *XP85012 Datasheet*, tech. rep., 2013.
- [48] E. Delagnes, D. Breton, H. Grabas, J. Maalmi and P. Rusquart, *Reaching a few picosecond timing precision with the 16-channel digitizer and timestamper SAMPIC ASIC*, *Nuclear Instruments and Methods in Physics Research Section A* **787** (2015) 245–249.
- [49] D. Breton, V. De Cacqueray, E. Delagnes, H. Grabas, J. Maalmi, N. Minafra et al., *Measurements of timing resolution of ultra-fast silicon detectors with the SAMPIC waveform digitizer*, *Nuclear Instruments and Methods in Physics Research, Section A* **835** (2016) 51–60.
- [50] Cargille Laboratories Inc., *Technical Data Sheet for Meltmount Media 1.704, code 5870*, tech. rep., 2015.
- [51] D. Motta and S. Schonert, *Optical properties of Bialkali photocathodes*, *Nuclear Instruments and Methods in Physics Research Section A* **A539** (2005) 217–235, [physics/0408075].
- [52] S. Hirose, T. Iijima, K. Inami, D. Furumura, T. Hayakawa, Y. Kato et al., *Development of the micro-channel plate photomultiplier for the Belle II time-of-propagation counter*, *Nuclear Instruments and Methods in Physics Research Section A* **787** (2015) 293–296.
- [53] A. Y. Barnyakov, M. Y. Barnyakov, D. A. Cygankov, A. A. Katcin, S. A. Kononov and A. P. Onuchin, *Measurement of the photoelectron collection efficiency in MCP PMT*, *Journal of Instrumentation* **12** (2017) P03027.
- [54] Advanced Laser Diode System A.L.S. GmbH, *Picosecond Diode Laser - Pilas, Manual and Test Report CEA PiL040XSM-1_825*, tech. rep., 2017.
- [55] Zaber Technologies Inc., *X-LRT-C Series User's Manual*, tech. rep., 2017.
- [56] S. Korpar, P. Križan, R. Pestotnik and A. Stanovnik, *Timing and cross-talk properties of BURLE multi-channel MCP PMTs*, *Nuclear Instruments and Methods in Physics Research Section A* **595** (2008) 169–172.

- [57] A. Lehmann et al., *Lifetime of MCP-PMTs and other performance features*, *Journal of Instrumentation* **13** (2018) C02010.
- [58] V. A. Li, J. Koblanski, R. Dorrill, M. J. Duvall, K. Engel, G. R. Jocher et al., *Studies of MCP-PMTs in the miniTimeCube neutrino detector*, *arXiv* (2018) , [1809.08314].
- [59] K. Inami, T. Mori, T. Matsumura, K. Kurimoto, S. Hasegawa, Y. Suzuki et al., *Cross-talk suppressed multi-anode MCP-PMT*, *Nuclear Instruments and Methods in Physics Research Section A* **592** (2008) 247–253.
- [60] V. A. Grigoryev, V. A. Kaplin, T. L. Karavicheva, A. B. Kurepin, E. F. Maklyae, Y. A. Melikyan et al., *Study of the Planacon XP85012 photomultiplier characteristics for its use in a Cherenkov detector*, *J. Phys. Conf. Ser.* **675** (2016) 042016.
- [61] A. Levin and C. Moisan, *A more physical approach to model the surface treatment of scintillation counters and its implementation into DETECT*, *1996 IEEE Nuclear Science Symposium. Conference Record* **2** (1996) 702–706 vol.2.
- [62] M. Alokhina, C. Canot, O. Bezshyyko, I. Kadenko, G. Tauzin, D. Yvon et al., *Simulation and Optimization of the Cherenkov TOF Whole-Body PET Scanner*, *Nuclear Instruments and Methods in Physics Research, Section A* **912** (2018) 378 – 381.
- [63] M. Alokhina, *Design of the Cherenkov TOF whole-body PET scanner using GATE simulation*. PhD thesis, Université Paris-Saclay ; Taras Shevchenko National University of Kyiv, 2018.
- [64] D. A. Orlov, J. DeFazio, S. D. Pinto, R. Glazenberg and E. Kernén, *High quantum efficiency S-20 photocathodes in photon counting detectors*, *Journal of Instrumentation* **11** (2016) C04015–C04015.
- [65] D. Yvon, *Detecteur de photons a haute energie, (High energy photon detector)*, CEA Patent, Ref: N1361037, BD15034SG, 12 november 2013.
- [66] H. Moriceau, F. Rieutord, F. Fournel, L. D. Cioccio, C. Moulet, L. Libralesso et al., *Low temperature direct bonding: An attractive technique for heterostructures build-up*, *Microelectronics Reliability* **52** (2012) 331 – 341.
- [67] D. Yvon and V. Sharyy, *Detector of high energy photons*, CEA Patent, Ref: FR3071930, 29 september 2017.